Ceramics International 48 (2022) 17440–17448

Contents lists available at ScienceDirect

Ceramics International

journal homepage: www.elsevier.com/locate/ceramint

Magneto-inductive open-cell cellular carbon composites with activated carbon as guest phase: Guefoams for energy-efficient VOCs management

J.M. Molina-Jordá

Department of Inorganic Chemistry and University Materials Institute of Alicante, University of Alicante, Ap-99, E, 03080, Alicante, Spain

ARTICLE INFO

Keywords:
B
Composites
C
Magnetic properties
D
Carbon
E
Functional applications

ABSTRACT

Guefoams (guest-containing foams) are a new-class of open-cell cellular materials that extend the properties of conventional foams by incorporating guest phases that convert them into multifunctional materials. This manuscript describes the development of pitch-derived composite guefoams that contain two types of inclusions: iron nanoparticles embedded in the cellular skeleton and activated carbon particles as guest phases. The activated carbon particles significantly increase the specific surface area and gas adsorption capacity. When these materials are exposed to low-intensity magnetic fields, the iron nanoparticles confer a high magneto-inductive capacity that enables ultrafast heating and rapid desorption of adsorbed species. The ability of these materials to act as preconcentrators for volatile organic compounds (VOCs) is demonstrated in this work using toluene as a proof of concept. The Guefoams developed here have greater preconcentration capabilities than current state-of-the-art systems while also being significantly more energy efficient due to the magnetic induction controlled desorption process. This unparalleled blend of properties makes these guefoams a valuable tool for energy-efficient VOCs management.

1. Introduction

For years, open-cell cellular materials have been used in many emerging thermal, catalytic and biomedical applications due to their mechanical and heat transfer properties and the fact that fluids can flow through and interact with them for specific purposes [1–4]. However, the cellular materials developed to date have such a low specific surface area that their potential use in adsorption/desorption of hazardous chemicals or pollutants has been scarcely explored. In fact, we find in the literature a reduced number of attempts in which cellular materials have been tested for these applications. These attempts are mainly based on two approaches: preparation of cellular solids from adsorbent materials or integration of adsorbent materials into cellular structures. Following the first approach, we highlight the proposal presented in Ref. [5] to use nanoporous materials such as mesostructured silica to form macroporous ordered cellular materials with nanometer-scale porosity. These structures have an interesting specific surface area (on the order of 200–550 m^2/g), but are not expected to have sufficient mechanical properties to be used without the aid of a support material. It is also worth mentioning recent work with carbon nanotube sponges, for which low specific surface areas of less than 100 m^2/g have been measured [6,7]. The second alternative, based on the integration of adsorbent materials into cellular solids, has also not produced a breakthrough milestone. The authors of [8,9] used cellular polymers loaded with activated carbon particles. This idea was not pursued due to the low adsorption capacity of the final material, as the matrix blocks access to the active adsorption sites of the loading material. More successful were the materials developed in Ref. [10] for photocatalytic applications, where the adsorption of volatile organic compounds (VOCs) is performed on titanium dioxide nanoparticles deposited on cellular nickel. In this case, relatively large specific surface areas were achieved (300 m^2/g), but the adsorption capacities were limited by the presence of moisture, which competed with the VOCs for the adsorption sites available on the titanium dioxide. On the line of combining cellular solids with adsorbent materials, some promising materials, called Guefoams (guest-containing foams), with specific surface areas larger than 300 m^2/g have been recently developed [11–13]. These materials consist of open-cell cellular aluminum containing both steel particles and activated carbon particles, which are hosted in the pores as guest phases and do not bond with the host cellular matrix except by mere physical contact.

In this work, novel mesophase pitch-derived open-cell cellular carbon composites of the new Guefoam family are developed. The Guefoams prepared here contain two types of inclusions at different

E-mail address: jmmj@ua.es.

https://doi.org/10.1016/j.ceramint.2022.03.008
Received 14 December 2021; Received in revised form 15 February 2022; Accepted 1 March 2022
Available online 9 March 2022

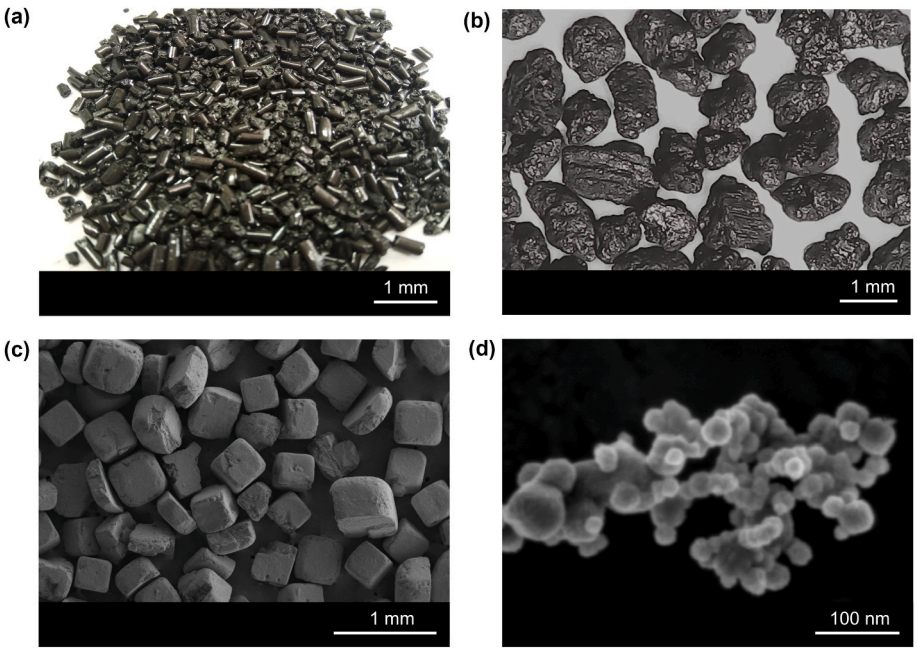

Fig. 1. Optical image of mesophase pitch pellets (a); SEM image of activated carbon particles (b); SEM image of NaCl particles (c); and FESEM image of Fe nanoparticles (d).

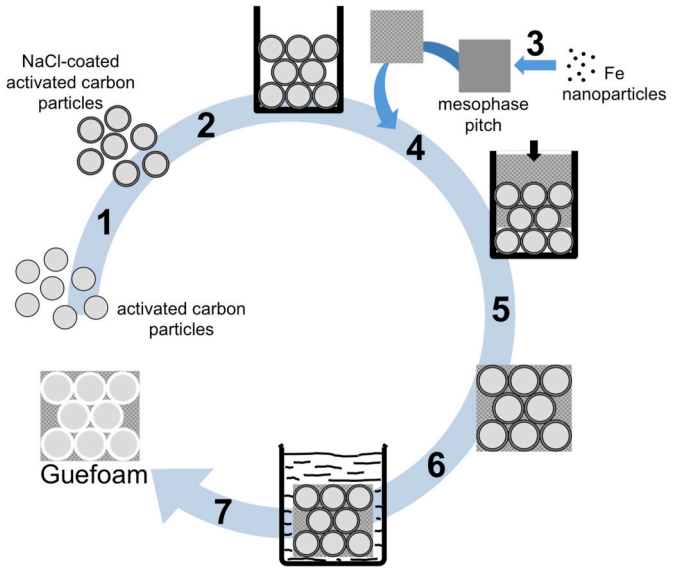

Fig. 2. Main steps in the preparation of the Guefoams in this work: 1 - coating of activated carbon particles with NaCl; 2 - packaging of the resulting particles; 3 - incorporation of Fe nanoparticles into the mesophase pitch; 4 - infiltration of the packed preform with the Fe nanoparticle-containing mesophase pitch; 5 - demolding of the infiltrated material, which is a composite material at this stage; 6 - dissolution of the NaCl coating; and 7 – heat treatments to stabilize and carbonize the matrix.

locations. On the one hand, iron nanoparticles embedded in the cellular skeleton transform these materials into magneto-inductive cellular composites. On the other hand, activated carbon particles with high specific surface area are hosted in cellular cavities as guest phases. Compared to Ref. [13], this new particle distribution, where all cavities accommodate high specific surface area guest phases and Fe nanoparticles are in intimate contact with the matrix, makes these cellular composites outstandingly adsorbent (with specific surface areas close to 500 m^2/g) and capable of rapidly desorbing substances by low power inductive heating. Such a blend of properties, not previously achieved in any other cellular solid, makes these materials very attractive for eco-friendly applications in the preconcentration and management of pollutants and hazardous chemical species.

2. Experimental procedures

2.1. Materials

Mitsubishi AR24 synthetic naphthalene-based mesophase pitch, kindly provided in pellet form by Mitsubishi Gas Chemical Company Inc. (Tokyo, Japan), was used as a precursor for the cellular carbon (Fig. 1a). We used Nuchar RGC-30 activated carbon (Westvaco - Chemical Division, Covington, VA, USA) with an average diameter of 1.2 mm as the guest phase particles (Fig. 1b). NaCl particles (99.9% purity) with a size of 400–500 μm (Fig. 1c) were purchased from NaCl AppliChem GmbH (Germany) and used as raw material for coating the activated carbon particles. Iron nanoparticles (Fig. 1d) were 40–60 nm in diameter and were purchased from Sigma-Aldrich (Riedstr, Switzerland).

2.2. Guefoam fabrication process

The Guefoam fabrication process is outlined in Fig. 2. It essentially consists of infiltrating a packed bed of NaCl-coated guest particles with a suitable liquid precursor and then removing the NaCl coating by water dissolution. For this purpose, activated carbon particles were coated with NaCl to an average thickness of about 0.12 mm by spray deposition from a 20 wt% aqueous NaCl solution [13]. The NaCl coating was subjected to recrystallization heat treatment in a horizontal furnace with an inert argon atmosphere. The treatment consisted of raising the temperature to 1068 K for 2 h, holding this temperature for 2.5 h and cooling to 298 K in 60 h. The slow cooling rate prevented the formation of cracks on the surface (see Ref. [13] for examples of cracking of NaCl coatings at faster cooling conditions after a similar heat treatment recrystallization process). Particles were packed to their maximum volume fraction in 17 mm diameter glass crucibles by a gentle process combining vibrations and impacts, attaining a particle volume fraction of about 0.62.

The embedding of iron nanoparticles in the mesophase pitch was

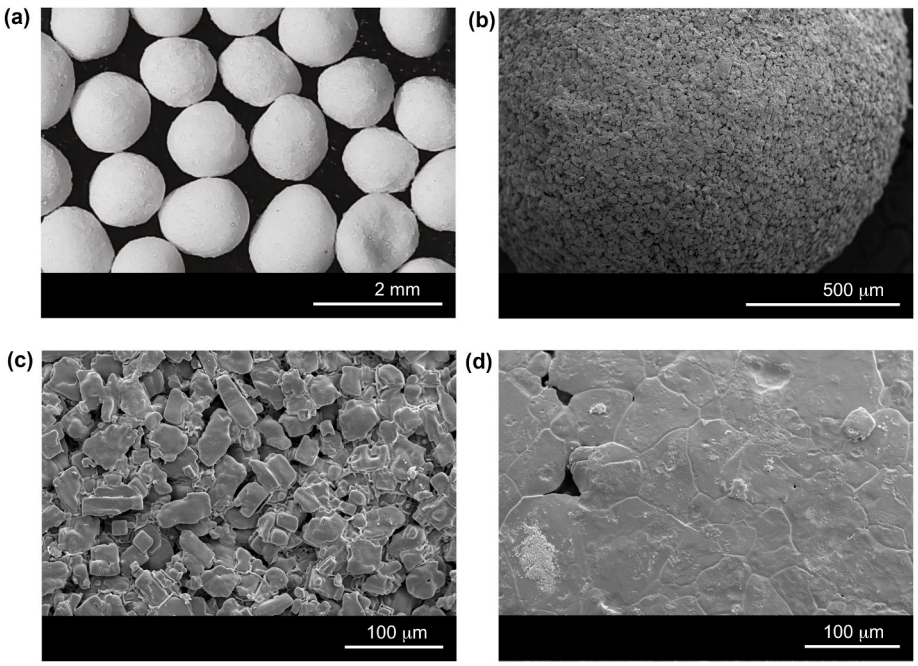

Fig. 3. Optical image of NaCl-coated activated carbon particles (a) and SEM micrograph of the surface of a particle (b); (c) and (d) are SEM micrographs of the topography of the NaCl surface before (c) and after (d) recrystallization treatment.

achieved by the following procedure: (i) Fe nanoparticles were mixed with mesophase pitch in the desired ratio in a flask reactor; (ii) toluene was added in a weight ratio of 25:75 mesophase pitch:toluene; (iii) the mixture was homogenized with a mechanical blade stirring system for 1 h; (iv) the reactor was sonicated for 1 h while mechanical stirring was maintained; and (v) the toluene was evaporated by magnetic stirring until a dry mixture was obtained. To obtain a toluene-free material, the Fe nanoparticle-containing mesophase pitch was melted and mechanically stirred for 1 h, then solidified and subsequently ball-milled. For detailed descriptions of the nanoparticle embedding process and infiltration with nanoparticle-containing mesophase pitch, see Ref. [14]. The investigated proportions of Fe nanoparticles in the pitch were 0%, 15% and 45% by volume.

The packed preforms conformed by the NaCl-coated activated carbon particles were argon pressure infiltrated at 1 bar with Fe nanoparticle-containing mesophase pitch at 633 K. For comparison, mesophase pitch without Fe nanoparticle content was also used as infiltration liquid precursor. After solidification of the mesophase pitch, the NaCl coating was dissolved by immersing the samples in water at 313 K with magnetic stirring. In a final step, the pitch matrix was stabilized under air atmosphere at 443 K for several hours and later carbonized at 1123 K in a horizontal quartz furnace with 10 ml/min nitrogen flow atmosphere.

2.3. Materials characterization

The structural features of the raw materials and Guefoams were studied using an Olympus PME-3 optical microscope, a Hitachi - S3000 N Scanning Electron Microscope (SEM) and a Zeiss – MerlinVP Field Emission Scanning Electron Microscope (FESEM). Nitrogen adsorption isotherms were determined in an Autosorb 6b Quantachrome Instruments facility (Florida, USA) at 77 K and evaluated according to the theory of Brunnauer, Emmett and Teller (BET) [15]. Selected samples were also characterized by X-ray diffraction (Bruker D8-Advance with monochromatic Cu-Ka radiation at a scanning 2θ between 10 and 100°. Magnetic properties were measured using an AMH-DC-TB-S permeameter from Laboratorio Elettrofisico (Italy), which allowed measurements on large samples with cylindrical geometry.

Table 1
Average diameter D (in mm) of the particulate. D(x) is the diameter (also in mm) below which x % of the particles are found. The span of the size distribution is defined as [D(90)-D(10)]/D(50). The circularity factor is defined as $4 \cdot \pi \cdot \text{area}/\text{perimeter}^2$, where 1.0 indicates a perfect circle. All results were obtained from measurements of over 300 particles. For more information on these measurements, see Supplementary Material (Figs. S1 and S2).

particulate	D	D(10)	D(90)	span	circularity
activated carbon	1.23	1.01	1.46	0.37	0.68
NaCl-coated activated carbon	1.47	1.36	1.57	0.14	0.90

3. Results and discussion

Fig. 3a and b shows images of the activated carbon particles after coating with NaCl. The coating has several effects that are worth commenting. Besides increasing the average diameter of the particles, which changes from 1.2 mm to about 1.5 mm, it homogenizes their size, as the span of their distribution is significantly reduced (see Table 1 and Fig. S1 of Supplementary Material). At the same time, the coating process leads to a spheroidization of the particles, which change from angular shapes in the case of activated carbon to round shapes in the case of NaCl-coated activated carbon (the circularity, measured in projection images of the particles, increases by 30% after coating) (see Table 1 and Fig. S2 of Supplementary Material).

Fig. 3c and d shows close-up images of the surface of the NaCl coating before and after recrystallization treatment, respectively. Before treatment, the coating consists of cube-shaped crystals with a maximum diameter of 30–50 μm and has a porous and rough surface. After treatment, the result is a much less porous surface with virtually no roughness, in which large grains with a maximum diameter between 40 and 100 μm can be observed. This new surface microstructure ensures the impenetrability by the liquid pitch during the infiltration process, which would otherwise infiltrate the NaCl coating due to its high wetting capacity [16]. Note that this is not the case in the fabrication of metal matrix Guefoams due to the limited wetting capacity of metals, which do not infiltrate the NaCl coating at the commonly used infiltration pressures [13].

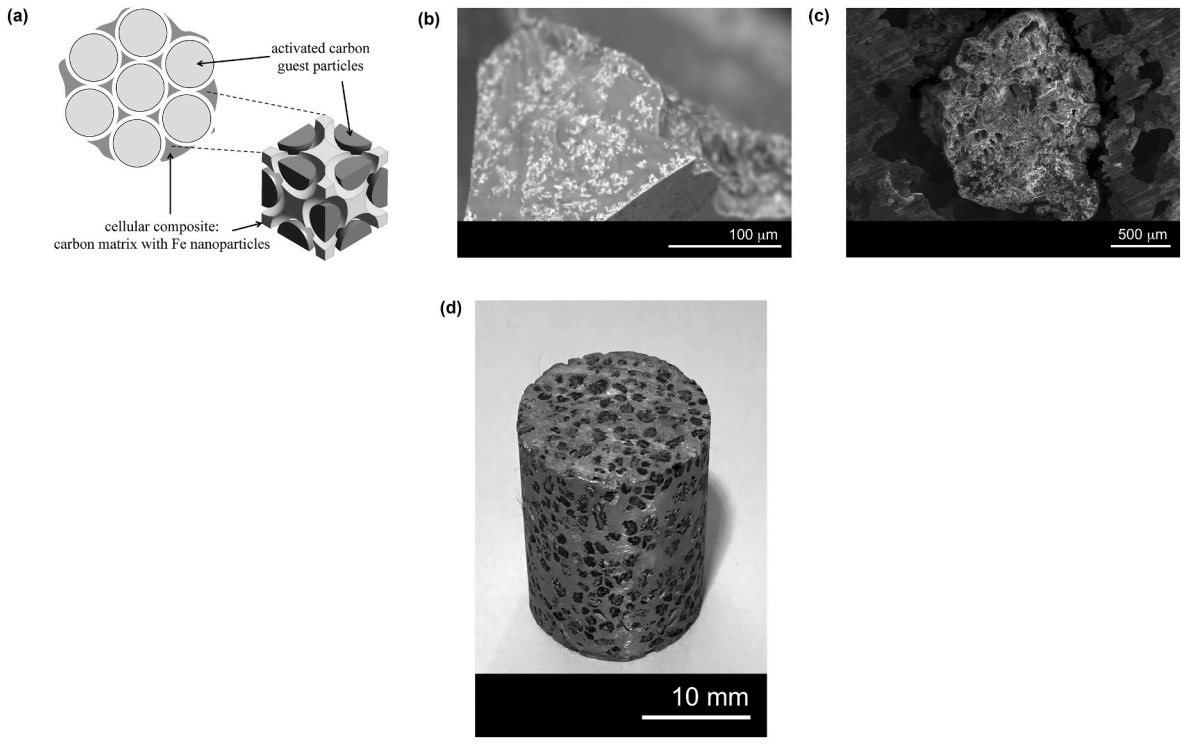

Fig. 4. (a) General structure of the Guefoams developed here; (b) SEM image of the strut of a cellular mesophase pith containing 45 vol% Fe nanoparticles; (c) SEM image showing an activated carbon particle as a guest phase hosted in a cellular cavity in sample C-nFe$_{45}$-[C$_a$]; and (d) photograph of a Guefoam specimen (sample C-nFe$_{45}$-[C$_a$]).

Table 2
Samples prepared in this study and their main properties: Guest occupation (GO) and guest loading (GL) as in Equations (1) and (2) and Ref. [13], specific surface area (S_{BET} in m^2/g) and magnetic parameters - M_s and M_r (both in emu/g) are the saturation and remanent magnetizations, respectively, and H_c (in Oe) is the magnetic coercitivity. Sample codes: C-nFe$_x$ are carbon matrix (C) foams containing x volume percent iron nanoparticles (nFe); C-nFe$_X$-[C$_a$] represents Guefoams containing activated carbon particles (C$_a$) as guest phases. For more information on the GL measurement, see Supplementary Material (Fig. S3).

Sample	GL (%) (±1)	GO (%) (±1)	volume fraction (±0.02)				S_{BET}	M_s	M_r	H_c
			C_{matrix}	C_a	Fe	Pores				
activated carbon (C$_a$)	–	–	–	–	–	–	1385	–	–	–
C-nFe$_0$ (C$_{foam}$)	0	0	0.38	0.00	0.00	0.62	0.10	–	–	–
C-nFe$_{15}$			0.32		0.06		0.11	21	3.1	141
C-nFe$_{45}$			0.21		0.17		0.13	52	9.4	139
C-nFe$_0$-[C$_a$]	97	58	0.38	0.36	0.00	0.26	483	–	–	–
C-nFe$_{15}$-[C$_a$]			0.32		0.06		495	18	3.2	139
C-nFe$_{45}$-[C$_a$]			0.21		0.17		479	54	10	138

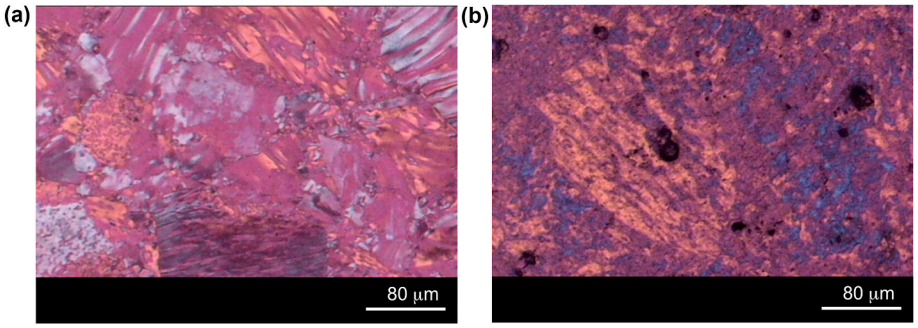

Fig. 5. Optical images of the mesophase pitch microstructure after infiltration (images of the upper residual material on the preform after infiltration) under two conditions: (a) without embedded nanoparticles and (b) with embedded 45 vol% Fe nanoparticles.

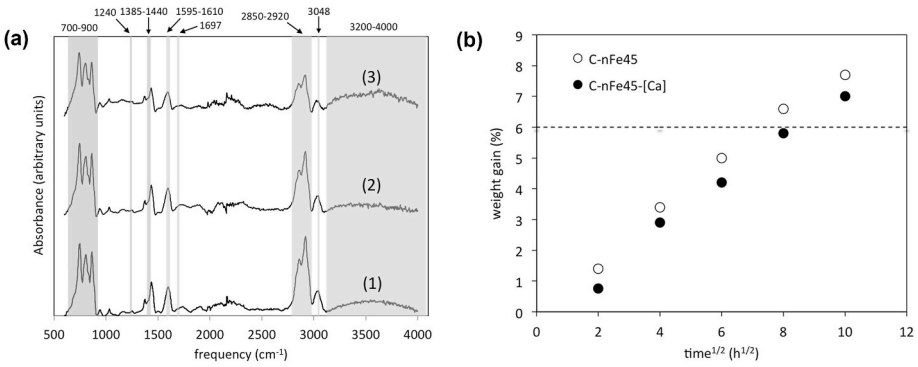

Fig. 6. (a) IR spectra of pitch under the following conditions: As-received (AR – spectrum 1), after the nanoparticle incorporation treatment series (ARt – spectrum 2), and with 15% Fe nanoparticles after stabilization at 443 K for 60 h (ARs-15nFe –spectrum 3); and (b) weight gain as a function of heat treatment time for two samples during stabilization treatment in forced synthetic air atmosphere at 443 K - the dashed line marks a 6% weight gain for which the pitch is considered stabilized.

Fig. 4a shows a sketch of the general structure of Guefoams and illustrates that guest phase particles are hosted in the cellular cavities without bonding with the cellular solid except by mere physical contact. For the Fe-containing samples, it is important that the nanoparticles are well dispersed in the carbonaceous matrix, as shown in Fig. 4b for a fresh fractured strut of a cellular mesophase pitch containing 45 vol% Fe nanoparticles. Fig. 4c is a micrograph showing the remaining space between the guest phase and the cellular skeleton in a Guefoam specimen (sample C-nFe$_{45}$-[C$_a$] – see Table 2 for the different materials prepared in this work). The samples prepared in this work have the maximum dimensions shown in Fig. 4d.

The procedure for incorporating Fe nanoparticles into mesophase pitch consists of their partial dissolution in toluene, followed by heat treatments to remove the solvent [14]. These treatments can induce changes in the mesophase pitch that can significantly alter its physicochemical properties [17]. Fig. 5 shows the changes in the crystal structure of mesophase pitch due to the incorporation of Fe nanoparticles. The absence of nanoparticles allows the growth of larger crystalline domains corresponding to the characteristic microstructures of AR24 mesophase pitch, which is identified as a pnematic liquid crystal [17]. To investigate the possible chemical changes in detail, the mesophase pitch was subjected to the same series of treatments used for the incorporation of the Fe nanoparticles and analysed by Infrared Spectroscopy (IR) (ARt – spectrum 2 of Fig. 6a). For comparison, Fig. 6a also shows the IR spectrum of the as-received AR24 mesophase pitch (AR – spectrum 1).

Both IR spectra for AR and ARt samples show characteristic vibrational bands of aromatic C–H bonds (at 3048 and 700-900 cm^{-1}) and aliphatic C–H bonds (at 2850–2920 and 1385-1440 cm^{-1}). Bands corresponding to the bending vibrations of polyaromatic C–C bonds (at 1595-1610 cm^{-1}) are also detected. There is also a broad band at 3200-4000 cm^{-1} corresponding to stretching vibrations in N–H and O–H groups, the latter mainly due to surface functionalization of the pitch. Another smaller band at 1687 cm^{-1} is characteristic of the C–O vibrations in aryl ketones or aryl aldehydes. The most obvious difference between the two spectra of samples AR and ARt is the lower intensity of the bands in sample ARt, particularly at 2850-2920 cm^{-1}, 3048 cm^{-1} and 3200-4000 cm^{-1}. The bands at 700–900 and 1385-1440 cm^{-1} have also lost intensity, although in these cases the changes are less apparent. These changes are likely a consequence of the process of solvent evaporation during the nanoparticle incorporation treatments, which can lead to simultaneous evaporation of the more volatile species of the pitch corresponding to low molecular weight units. This would justify the lower intensity in the ARt spectrum of the characteristic bands at 2850-2920 cm^{-1} and 3040 cm^{-1} of the aromatic and aliphatic C–H bonds, respectively. The lower intensity of the band at 3200-4000 cm^{-1} in the ARt could be due to a loss of O–H groups in the pitch by a process of surface defunctionalization. Similar chemical changes were also reported in Ref. [17] for a mesophase pitch of the same origin as the one used in the present work, in which TiC nanoparticles were incorporated. It was shown in Ref. [17] that these chemical changes have no clear correlation with variations in the softening point of the pitch, but that the nanoparticle content affects the viscosity derived from pressure-assisted infiltration experiments. These facts indicate that the chemical changes occurring in the pitch during nanoparticle incorporation do not significantly affect its intrinsic properties and that the changes in viscosity are mainly due to fluid dynamic effects resulting from the presence of the nanoparticles.

The stabilization treatment of mesophase pitch (alternatively called thermosetting) is a necessary step in the processing methodology if the dimensionality of the material is to be maintained. During stabilization, oxygen diffusion and various chemical reactions cause crosslinking of the polymer chains of the pitch, the properties of which depend on temperature and treatment time [18,19]. This heat treatment, carried out here at low temperature (443 K) in an air atmosphere (following [20]), is characterized by a weight increase of the pitch and can be considered complete when this weight increase is about 6%.

Fig. 6b shows the pitch weight variation with stabilization treatment time for a Guefoam specimen (sample C-nFe$_{45}$-[C$_a$]) and its equivalent cellular solid without guest phases (sample C-nFe$_{45}$). Some differences can be appreciated between the two materials, indicating a greater difficulty in stabilization in the Guefoam materials, likely caused by the greater difficulty of air passage through the material due to the presence of guest phases in the voids. This stabilization treatment is completed after about 60 h (shorter stabilization times could be achieved by an alternative procedure using a compressed air stream [21]) and leads to additional changes in the infrared spectrum profile, as shown in Fig. 6a for a stabilized pitch sample with 15% Fe nanoparticles (ARs-15nFe – spectrum 3). The IR spectrum of the stabilized sample illustrates the enrichment of the pitch with oxygen during the thermosetting process. Firstly, there is a significant decrease in the intensity of the vibrational bands of the aliphatic C–H bonds. Moreover, a relatively broad band around 1240 cm^{-1} gains intensity, which is almost absent in non-oxidized samples and corresponds to the asymmetric vibrations of the C–O–C ether groups. Finally, the band at 3200-4000 cm^{-1}, which is responsible for the vibrations of the O–H bonds and which had lost intensity due to the incorporation of the nanoparticles, regains intensity due to the stabilization process.

Table 2 lists the main adsorption and magnetic properties of the different samples prepared in this work. The definition of Guest Occupation (GO) and Guest Loading (GL) are as follows:

$$GL(\%) = \frac{number\ of\ pores\ hosting\ guest\ phases}{total\ number\ of\ pores} \times 100 \quad (1)$$

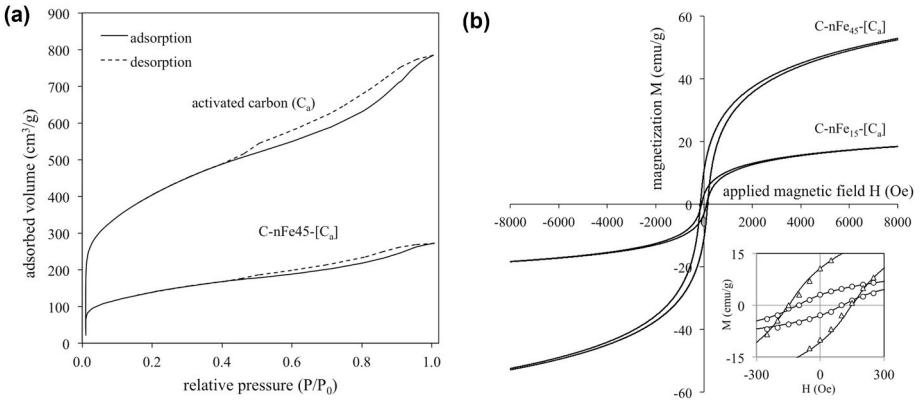

Fig. 7. (a) Nitrogen adsorption isotherms (volume per unit mass versus relative pressure P/P_o where P_o is the saturation pressure) for activated carbon particles and the C-nFe$_{45}$-[C$_a$] Guefoam; and (b) magnetization curves for the C-nFe$_{15}$-[C$_a$] and C-nFe$_{45}$-[C$_a$] Guefoams.

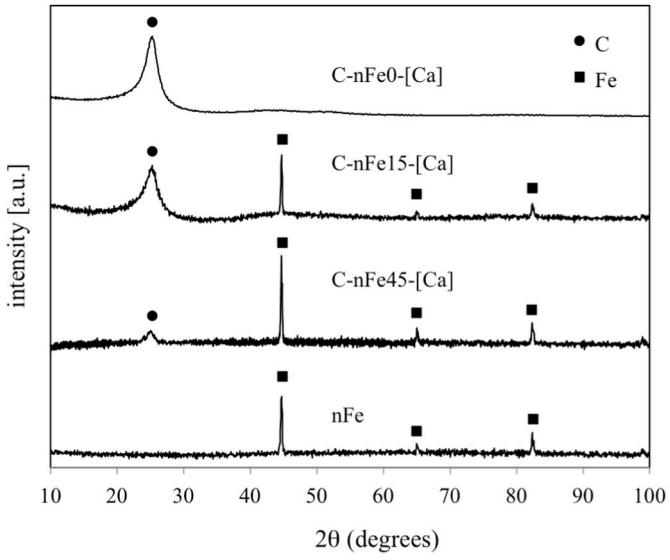

Fig. 8. X-ray diffractograms for samples C-nFe$_0$–[C$_a$], C-nFe$_{15}$-[C$_a$], C-nFe$_{45}$-[C$_a$] and nFe (as-received iron nanoparticles).

$$GO(\%) = \frac{average\ volume\ of\ guest\ specimens}{average\ volume\ of\ hosting\ pores} \times 100 \quad (2)$$

Measurements of GL were performed as indicated in Supplementary Material (Fig. S3). The parameter GO was calculated based on the average size of the activated carbon and NaCl-coated activated carbon particles. The specific surface area (S_{BET}) of Guefoams is high compared to standard cellular carbon (C_{foam}) due to the high adsorption capacity of the activated carbon particles (Fig. 7a). The S_{BET} for Guefoams is fairly constant as they all have the same values for GL and GO (Table 2). Thus, the presence of Fe nanoparticles has no detectable effect on the S_{BET} since the nanoparticles are embedded in the carbonaceous matrix. However, the Fe nanoparticles confer magnetic properties to the materials (Table 2 and magnetization curves in Fig. 7b). The magnetic properties of Fe nanoparticles have been tested in the literature [22], as well as their inductive heating effects when incorporated into polymer matrices [23–25]. The possibility that Fe nanoparticles can be surface oxidized during pitch stabilization was investigated by X-ray diffraction (Fig. 8) The diffraction patterns of the C-nFe$_0$–[C$_a$], C-nFe$_{15}$-[C$_a$], C-nFe$_{45}$-[C$_a$] and nFe (as-received iron nanoparticles) samples all show peaks associated with mesophase pitch and native Fe, indicating that any oxide formed on the particles, either naturally or as a result of the stabilization process, is negligible. Had these particles undergone significant oxidation, no loss of properties would have been expected, since it was shown in Ref. [26] that the two most stable iron oxides (Fe_2O_3 and Fe_3O_4) that can be formed by iron during oxidative processes can contribute to a larger induction effect and thus to a higher heating rate. The absence of peaks associated with NaCl confirms that NaCl was completely dissolved during the preparation of these materials, which

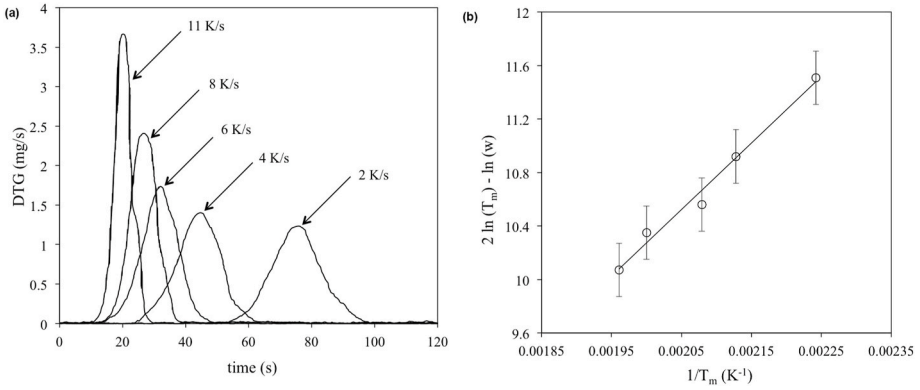

Fig. 9. (a) DTG curves for the desorption of toluene at different heating rates of C-nFe$_{45}$-[C$_a$] Guefoam subjected to magnetic fields with a frequency of 450 kHz and different induction powers; and (b) plot of $2\ln(T_m) - \ln(w)$ versus $1/T_m$ - the straight line fitting the data is $2\ln(T_m) - \ln(w) = 4178.8 \cdot (1/T_m) + 1.7529$, with a regression coefficient >0.99.

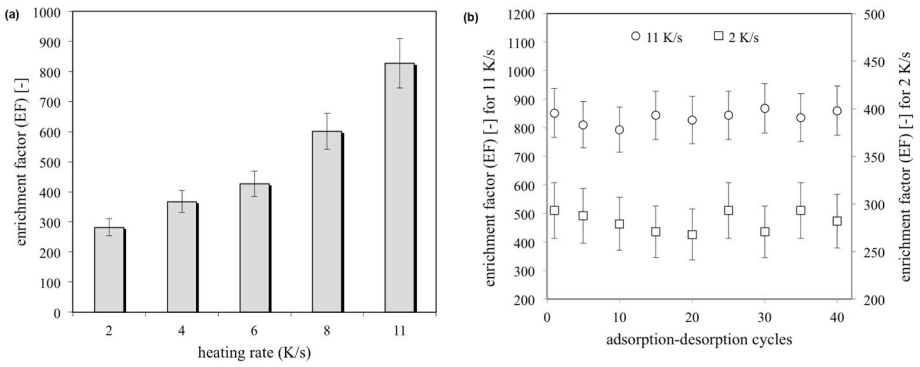

Fig. 10. (a) Enrichment factor as a function of heating rate for the C-nFe$_{45}$-[C$_a$] Guefoam, and (b) enrichment factor for two nominal heating rates of 11 and 2 K/s as a function of the number of adsorption-desorption cycles for the C-nFe$_{45}$-[C$_a$] Guefoam.

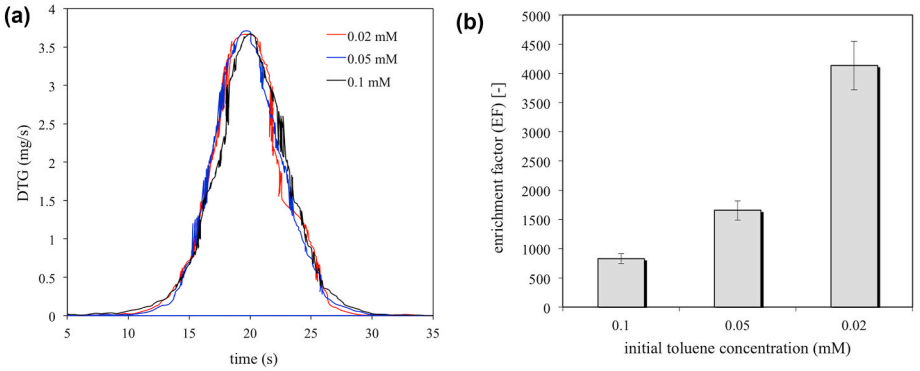

Fig. 11. (a) DTG curves for the desorption of toluene previously adsorbed on Guefoam C-nFe45-[Ca] at a heating rate of 11 K/s, employing different initial toluene concentrations (0.02 mM, 0.05 mM and 0.10 mM); and (b) enrichment factor as a function of initial toluene concentration for C-nFe45-[Ca] Guefoam.

can be characterized as cellular materials with 100% open cells. The sample C-nFe$_{45}$-[C$_a$], which has the highest content of Fe nanoparticles, combines high S_{BET} with high magnetic properties. These magnetic properties are reflected in high magnetic induction heating rates, which can be as high as 11 K/s for the C-nFe$_{45}$-[C$_a$] sample when subjected to a magnetic field with a frequency of 450 kHz at a power consumption of 44 W.

As proof of concept, toluene was adsorbed on specimens of C-nFe$_{45}$-[C$_a$] with reduced dimensions of 22 mm in length and 5 mm in diameter by flowing nitrogen carrier gas at 298 K and 450 ml/min with an inlet concentration of 0.10 mmol/l toluene for 24 h. Samples were then subjected to differential thermogravimetry (DTG) using a thermobalance (Setaram TGA-92) coupled to a magnetic induction device that allows adjustable sample heating rates by operating at 450 kHz and different induction powers. A helium gas flow of 10 ml/min was used during desorption. The DTG results (Fig. 9a) confirmed that the toluene desorption from the activated carbon particles contained in C-nFe$_{45}$-[C$_a$] Guefoam was controlled by the heating rate, which in turn was determined by the magnetic induction capacity of the sample. From the collected data, the enthalpy for toluene desorption from the Nuchar RGC-30 activated carbon used here was derived by linear transformation of the well-known equation of Cvetanovic and Amenomiya, which was generalized in Ref. [27] for different experimental conditions. It consists of plotting $2\ln(T_m)-\ln(w)$ vs $(1/T_m)$, where T_m and w are the temperature of the maximum desorption rate (peak temperature in DTG) and the heating rate, respectively (Fig. 9b). Using this approach, a value of 41.3 kJ/mol was derived for the desorption of toluene from RGC-30 activated carbon (we assume that the energetic contribution of the cellular host is negligible due to its low specific surface area - see S_{BET} value for C_{foam} in Table 2). The value found is in close agreement with other reported values [28] for the desorption of toluene from activated carbon obtained by carbonizing dense wood (coconut wood was the raw material used for RGC-30 production), close to the heat of vaporization of toluene, nominally 33.4 kJ/mol [29], suggesting that no strong endo- or exothermic processes are involved during desorption.

From the heating rates achieved in the C-nFe$_{45}$-[Ca] sample, the toluene enrichment factors (EFs) can be calculated as the percentage ratio of the analyte (toluene) concentration in the desorbed gas to the analyte concentration in the carrier gas prior to adsorption in the preconcentrator system (Fig. 10a). These concentrations were determined by MTI P200H microchromatography considering the total time for complete desorption. The highest EF corresponds to the highest heating rate achieved (11 K/s) for which the EF determined a value over 800. Fig. 10b shows the behaviour of the C-nFe$_{45}$-[Ca] material in several adsorption-desorption cycles, where it was found that the enrichment factor remained constant up to 40 cycles tested.

It has been found that EF depends on factors as diverse as the volume and shape of the preconcentrator system, adsorption and desorption fluxes, pressure drop, and heating rate [30]. Fig. 10a highlights the positive effect of high heating rates on the increase of EF. To evaluate the effect of initial analyte concentration on EF, additional experiments were performed with initial concentrations of 0.05 mM and 0.02 mM toluene under the same conditions used so far (450 ml/min nitrogen flow during adsorption, 24 h adsorption time and 10 ml/min helium flow during desorption) at a heating rate of 11 K/s. The DTG curves (Fig. 11a) show similar desorption performance for the different concentrations evaluated. The EF (Fig. 11b) shows a strong dependence on the initial concentration, reaching values over 4000 for an initial toluene concentration of 0.02 mM.

These values are an important milestone among those found in the literature for the enrichment of VOCs in solid gas extraction systems with adsorption-desorption cycles. Depending on how the adsorbing

Table 3
Summary of directly heated preconcentrator systems reported in the literature for VOCs preconcentration. S_{BET} is the specific surface area in m^2/g; Q is the quantity of adsorbent in mg; ER stands for "electrical resistance" and refers to the heating system in which an electrical current is passed through a resistive element, which is specified in brackets; power refers to the power consumption in W, V is the heating rate in K/s; C_o is the initial concentration of adsorbate in ppb; F_{des} is the desorption flux in ml/min and EF, as described in this paper, is the enrichment factor. Where indicated, ND means "not disclosed".

Cavity layout[a]	Adsorbent			Heating			Sampling		EF	Ref.
	Material[b]	S_{BET}	Q	type	power	V	C_o	F_{des}		
SS	Serial packaging of GC	100–1200	12.3	ER (Pt)	ND	100	100	4	5000	[38]
Glass	Tenax	35	35	ER	6	4.2	70–18000	10	200	[39]
Chamber	Lab-made AC	250–2300	1–2.5	ER (Pt)	ND	8.3	150	ND	150–800	[40]
MEMS	AC, CNT, Tenax	21–399	ND	ER (Pt)	ND	2.7	-	33	60	[41]
MEMS	Cellulose-derived CF	308	2.0	ER (Au)	3.6	1	100	3	>13000	[42]
MEMS	CN	NS	1.0	ER	ND	5–160	10–500	33–166	60	[30]
Foil	Carbopack, Tenax	100	1.0	ER (Au)	1.7	40	250	66	8–200	[43]
MEMS	Tenax	35	7.0	ER	2.5	17.6	22–667	5–25	5–10	[44]
Glass	CNT-sponge	74	5.0	ER	39	481.5	100	6.5	50->800	[6,7]

[a] SS: stainless steel; MEMS: microelectromechanical system.
[b] GC: graphitized carbon; AC: activated carbon; CN: carbon nanopowder; CF: carbon film; CNT: carbon nanotubes.

substrate is heated, two basic preconcentration systems are distinguished in the literature. On the one hand, there are indirectly heated systems, in which a carrier gas at high temperature flows through a packed bed of adsorbent in the form of finely divided particles or fibres, thereby heating it and causing desorption. In these cases, the EF values are usually less than 50 because high gas fluxes are required for efficient heating [31]. Adsorbents include activated carbon, zeolites or mesoporous solids [32–35].

A second approach is to heat the adsorbent directly, which is the method used in the present work. In this case, the carrier gas flow can be reduced and the enrichment factor can be significantly increased (see Table 3 for a complete review of directly heated preconcentrator systems published in the literature). In general, EFs vary in the range of 5–800 for initial sample concentrations on the order of ppb (much lower than those used here) and desorption fluxes are in the range of 5–166 ml/min. Special cases include those published in Refs. [30,34], where EFs as high as 5000 and > 13000 are achieved by maximising heating rates above 100 K/s and minimising desorption fluxes to values as low as 4 and 3 ml/min, respectively. In Refs. [6,7], heating rates of more than 450 K/s and enrichment factors for toluene greater than 800 were achieved when carbon nanotube sponges were directly heated by electric current. In comparison to previously published materials, the guefoams developed here exhibit high enrichment factors despite the use of initial analyte concentrations at least one order of magnitude higher than those used in the references cited in Table 3. Indeed, if initial toluene concentrations on the order of 100 ppb had been used as in Refs. [30,34], the expected enrichment factors for heating rates of 2–11 K/s would have been in the range of 20000–80000 based on the measured desorption kinetics and a helium flow rate of 10 ml/min. Along with improved preconcentration performance, the proposed system is also characterized by its energy efficiency. A comparison between different systems in terms of energy efficiency is difficult given the specificities of each configuration in the variety of systems proposed. The systems in Table 3 are based on Joule heating of resistive elements, whose energy efficiency has been shown to be slightly more than half that of systems based on inductive heating [36,37]. In fact, the consumption powers of the systems in Table 3 (for the reported cases) vary in the range of 1.5–39 W for heating adsorbent quantities in the range of 1.0–7.0 mg. For the cellular materials in Refs. [6,7], which are structurally most similar to the materials developed in this work of all those in Table 3, 39 W are consumed in heating 5.0 mg of adsorbent. In the study presented here, a maximum power of 44 W is consumed to heat an amount of about 120 mg of adsorbent. It is therefore evident that the use of guefoams not only results in higher enrichment factors, but also enables the heating of larger amounts of adsorbent with excellent energy efficiency. In addition to these advantages, the use of guefoams brings other benefits on a more industrial use side, such as not requiring handling of particulate systems (which are best avoided for economic and health reasons) and the possibility to be produced in cost-effective batches on a large scale.

4. Conclusions

In summary, this article discusses the development of new open-cell cellular carbon composites from the recently emerged Guefoams family. These are cellular composites consisting of a carbon matrix with embedded iron nanoparticles and activated carbon particles as guest phase. These materials exhibit magneto-inductive and highly adsorptive properties that allow adsorption of volatile organic compounds (toluene was used as an example in this work) and rapid desorption using low-power magnetic fields, thus acting as effective preconcentrators with a higher performance than those currently available and are also more energy efficient due to their inductive rather than resistive heating. Due to their low energy consumption and high enrichment factors, these materials have important potential for the environmentally friendly preconcentration and management of VOCs.

Funding

This work was supported by the Spanish Agencia Estatal de Investigación (AEI), the Spanish Ministry of Science and Innovation, and the European Union (FEDER and NextGenerationEU funds) [grants MAT2016-77742-C2-2-P and PDC2021-121617-C21]. The author would also like to acknowledge the financial support received from the Conselleria d'Innovació, Universitats, Ciència, i Societat Digital of the Generalitat Valenciana through grant GVA-COVID19/2021/097.

Declaration of competing interest

The authors declare that they have no known competing financial interests or personal relationships that could have appeared to influence the work reported in this paper.

Acknowledgements

The author acknowledges L.P. Maiorano for fruitful discussions on the fabrication and characterization of the materials, as well as for a critical reading of the manuscript.

Appendix A. Supplementary data

Supplementary data to this article can be found online at https://doi.org/10.1016/j.ceramint.2022.03.008.

References

[1] K.C. Khemani, Polymeric foams: an overview, ACS Symp. Ser. 669 (1997) 1–7, https://doi.org/10.1021/bk-1997-0669.ch001.

[2] G. Lewis, Properties of open-cell porous metals and alloys for orthopaedic applications, J. Mater. Sci. Mater. Med. 24 (2013) 2293–2325, https://doi.org/10.1007/s10856-013-4998-y.

[3] E.C. Hammel, O.L. Ighodaro, O.I. Okoli, Processing and properties of advanced porous ceramics : an application based review, Ceram. Int. 40 (2014) 15351–15370, https://doi.org/10.1016/j.ceramint.2014.06.095.

[4] S. Singh, N. Bhatnagar, A survey of fabrication and application of metallic foams (1925–2017), J. Porous Mater. 25 (2018) 537–554, https://doi.org/10.1007/s10934-017-0467-1.

[5] H. Wang, X. Rong, L. Han, M. Tang, M. Yu, J. Zhang, W. Huang, R. Chen, Controlled synthesis of hexagonal mesostructure silica and macroporous ordered siliceous foams for VOCs adsorption, RSC Adv. 5 (2015) 5695–5703, https://doi.org/10.1039/c4ra12553c.

[6] J. Bang, D.W. You, Y. Jang, J.S. Oh, K.W. Jung, A carbon nanotube sponge as an adsorbent for vapor preconcentration of aromatic volatile organic compounds, J. Chromatogr., A 1605 (2019) 460363, https://doi.org/10.1016/j.chroma.2019.460363.

[7] Y. Jang, J. Bang, Y.S. Seon, D.W. You, J.S. Oh, K.W. Jung, Carbon nanotube sponges as an enrichment material for aromatic volatile organic compounds, J. Chromatogr., A 1617 (2020) 460840, https://doi.org/10.1016/j.chroma.2019.460840.

[8] W.M. Moe, R.L. Irvine, Polyurethane foam medium for biofiltration. I: Characterization, J. Environ. Eng. 126 (2000) 815–825.

[9] N. Correia, J.C.M. Bordado, J. Pires, M.B. Carvalho, A.P. Carvalho, M. Pinto, Open cell polyurethane foams for new filters with supported adsorbents, Mater. Sci. Forum 514–516 (2006) 892–896. https://dx.doi.org/10.4028/www.scientific.net/msf.514-516.892.

[10] A.H. Mamaghani, F. Haghighat, C.S. Lee, Gas phase adsorption of volatile organic compounds onto titanium dioxide photocatalysts, Chem. Eng. J. 337 (2018) 60–73, https://doi.org/10.1016/j.cej.2017.12.082.

[11] J.M. Molina-Jorda, Spanish Patent P201730890, 2017.

[12] J.M. Molina-Jorda, PCT Patent PCT/ES2018/070474, 2018.

[13] J.M. Molina-Jordá, Highly adsorptive and magneto-inductive guefoams (multifunctional guest-containing foams) for enhanced energy-efficient preconcentration and management of VOCs, ACS Appl. Mater. Interfaces 12 (2020) 11702–11712, https://doi.org/10.1021/acsami.9b22858.

[14] J.M. Molina-Jordá, Mesophase pitch-derived graphite foams with selective distribution of TiC nanoparticles for catalytic applications, Carbon N. Y. 103 (2016) 5–8, https://doi.org/10.1016/j.carbon.2016.02.051.

[15] S. Brunauer, L.S. Deming, W.E. Deming, E. Teller, On a theory of the van der Waals adsorption of gases, J. Am. Ceram. Soc. 62 (1940) 1723–1732, https://doi.org/10.1016/j.urology.2009.02.032.

[16] P.G. Wapner, W.P. Hoffman, R. Hurt, G. Krammer, Equilibrium and non-equilibrium effects in pitch wetting, in: Proc. Carbon 2003, 2003. Oviedo, Spain.

[17] J.M. Molina-Jordá, Insights into the flow behaviour of the AR24 mesophase pitch and nanoparticle-doped AR24 mesophase pitch during infiltration into particulate porous preforms, Carbon N. Y. 132 (2018) 451–465, https://doi.org/10.1016/j.carbon.2018.02.032.

[18] I. Mochida, Y. Korai, C.H. Ku, F. Watanabe, Y. Sakai, Chemistry of synthesis, structure, preparation and application of aromatic-derived mesophase pitch, Carbon N. Y. 38 (2000) 305–328, https://doi.org/10.1016/S0008-6223(99)00176-1.

[19] E.I. Andreikov, O.V. Krasnikova, O.V. Koryakova, Low-temperature oxidation of pitch, petroleum, and shale semicokes, Solid Fuel Chem. 44 (2010) 18–25, https://doi.org/10.3103/S0361521910010052.

[20] B. Fathollahi, B. Jones, P.C. Chau, J.L. White, Injection and stabilization of mesophase pitch in the fabrication of carbon-carbon composites. Part III: mesophase stabilization at low temperatures and elevated oxidation pressures, Carbon N. Y. 43 (2005) 143–151, https://doi.org/10.1016/j.carbon.2004.08.032.

[21] H. Shimanoe, S. Ko, Y.P. Jeon, K. Nakabayashi, J. Miyawaki, S.H. Yoon, Shortening stabilization time using pressurized air flow in manufacturing mesophase pitch-based carbon fiber, Polymers 11 (2019) 1–15, https://doi.org/10.3390/polym11121911.

[22] J. Carvell, E. Ayieta, A. Gavrin, R. Cheng, V.R. Shah, P. Sokol, Magnetic properties of iron nanoparticle, J. Appl. Phys. 107 (2010), https://doi.org/10.1063/1.3428415.

[23] C. Baker, S.I. Shah, S.K. Hasanain, Magnetic behavior of iron and iron-oxide nanoparticle/polymer composites, J. Magn. Magn Mater. 280 (2004) 412–418, https://doi.org/10.1016/j.jmmm.2004.03.037.

[24] T. Bayerl, M. Duhovic, P. Mitschang, D. Bhattacharyya, The heating of polymer composites by electromagnetic induction - a review, Composer Part A Appl. Sci. Manuf. 57 (2014) 27–40, https://doi.org/10.1016/j.compositesa.2013.10.024.

[25] J.L. Wilson, P. Poddar, N.A. Frey, H. Srikanth, K. Mohomed, J.P. Harmon, S. Kotha, J. Wachsmuth, Synthesis and magnetic properties of polymer nanocomposites with embedded iron nanoparticles, J. Appl. Phys. 95 (2004) 1439–1443, https://doi.org/10.1063/1.1637705.

[26] I. Baker, Q. Zeng, W. Li, C.R. Sullivan, Heat deposition in iron oxide and iron nanoparticles for localized hyperthermia, J. Appl. Phys. 99 (2006) 97–100, https://doi.org/10.1063/1.2171960.

[27] A. Jolly, J.P. Perrard, Determination of the heat of adsorption of ammonia on zeolites from temperature-programmed desorption experiments, Langmuir (2001) 1538–1542.

[28] C. Popescu, M. Joly, J.P. Danatoiu, Dynamical adsorption and temperature-programmed desorption of VOCs (toluene, butyl acetate and butanol) on activated carbons, Carbon N. Y. 41 (2003) 739–748, https://doi.org/10.1111/j.1365-2605.1998.00113.x.

[29] S.V. Majer V, Enthalpies of Vaporization of Organic Compounds: a Critical Review and Data Compilation, Blackwell, Oxford, 1985.

[30] M. Camara, P. Breuil, D. Briand, J.P. Viricelle, C. Pijolat, N.F. De Rooij, Preconcentration modeling for the optimization of a micro gas preconcentrator applied to environmental monitoring, Anal. Chem. 87 (2015) 4455–4463, https://doi.org/10.1021/acs.analchem.5b00400.

[31] H. Chmiel, E. Schippert, C. Möhner, European Patent EP001170050A1, 2002.

[32] C. Zhou, K. Zhou, H. Li, X. Xu, B. Liu, H. Li, Z. Zeng, W. Ma, L. Li, Pressure swing adsorption properties of activated carbon for methanol, acetone and toluene, Chem. Eng. J. (2020) 127384, https://doi.org/10.1016/j.cej.2020.127384.

[33] L. Xu, Y. Li, J. Zhu, Z. Liu, Removal of toluene by adsorption/desorption using ultra-stable Y zeolite, Trans. Tianjin Univ. 25 (2019) 312–321, https://doi.org/10.1007/s12209-019-00186-y.

[34] W. Jin, Y. Wang, X. Wang, L. Jin, J. Lu, M. Luo, Sorption properties of ordered mesoporous silica for toluene and ethyl acetate, Adsorpt. Sci. Technol. 29 (2011) 405–412, https://doi.org/10.1260/0263-6174.29.4.405.

[35] M. Woellner, S. Hausdorf, N. Klein, P. Mueller, M.W. Smith, S. Kaskel, Adsorption and detection of hazardous trace gases by metal–organic frameworks, Adv. Mater. 30 (2018) 1–27, https://doi.org/10.1002/adma.201704679.

[36] K. Frogner, M. Andersson, T. Cedell, L. Siesing, P. Jeppsson, J.E. Ståhl, Industrial heating using energy efficient induction technology Conference on Manufacturing Systems Total number of authors : induction technology, in: 44th CIRP Int. Conf. Manuf. Syst., 2011, pp. 1–6.

[37] E. Szychta, L. Szychta, Comparative analysis of effectiveness of resistance and induction turnout heating, Energies 13 (2020), https://doi.org/10.3390/en13205262.

[38] J.L. Chia, E.T. Zellers, Multi-adsorbent preconcentration/focusing module for portable-GC/microsensor-array analysis of complex vapor mixtures, Analyst 127 (2002) 1061–1068, https://doi.org/10.1039/b111689d.

[39] T. Hamacher, J. Niess, P. Schulze Lammers, B. Diekmann, P. Boeker, Online measurement of odorous gases close to the odour threshold with a QMB sensor system with an integrated preconcentration unit, Sensor. Actuator. B Chem. 95 (2003) 39–45, https://doi.org/10.1016/S0925-4005(03)00400-3.

[40] F. Blanco, X. Vilanova, V. Fierro, A. Celzard, P. Ivanov, E. Llobet, N. Cañellas, J. L. Ramírez, X. Correig, Fabrication and characterisation of microporous activated carbon-based pre-concentrators for benzene vapours, Sensor. Actuator. B Chem. 132 (2008) 90–98, https://doi.org/10.1016/j.snb.2008.01.016.

[41] E.H.M. Camara, P. Breuil, D. Briand, N.F. de Rooij, C. Pijolat, A micro gas preconcentrator with improved performance for pollution monitoring and explosives detection, Anal. Chim. Acta 688 (2011) 175–182, https://doi.org/10.1016/j.aca.2010.12.039.

[42] M.Y. Wong, W.R. Cheng, M.H. Liu, W.C. Tian, C.J. Lu, A preconcentrator chip employing μ-SPME array coated with in-situ-synthesized carbon adsorbent film for VOCs analysis, Talanta 101 (2012) 307–313, https://doi.org/10.1016/j.talanta.2012.09.031.

[43] M. Camara, P. Breuil, C. Pijolat, E. Hadji, M. Camara, P. Breuil, C. Pijolat, J. Viricelle, F. De Rooij, Tubular gas preconcentrators based on inkjet printed micro-hotplates on foil to cite this version : HAL Id : hal-01337348 Tubular gas preconcentrators based on inkjet printed micro- hotplates on foil, Sensor. Actuator. B Chem. 236 (2016) 1111–1117, j.snb.2016.06.121.

[44] M.M. McCartney, Y. Zrodnikov, A.G. Fung, M.K. Levasseur, J.M. Pedersen, K. O. Zamuruyev, A.A. Aksenov, N.J. Kenyon, C.E. Davis, An easy to manufacture micro gas preconcentrator for chemical sensing applications, ACS Sens. 2 (2017) 1167–1174, https://doi.org/10.1021/acssensors.7b00289.